3-D CFD simulation of oil shale drying in fluidized bed and experimental verification

Ruiting Dong, Liangzhi Xia*, Haonan Wang, Dongsheng Jiao

School of Chemical Engineering, Dalian University of Technology, Dalian, 116024, China

Abstract. *Fluidized bed drying is an economical and high-efficiency deep pre-dehydration technology for oil shale. The mature fluidized bed drying technology, which intensifies the retorting process, was applied to oil shale particles of high moisture content. The main objective of this paper was to explore the 3-D computational fluid dynamics (CFD) numerical simulation and experimental verification of oil shale particles drying in a fluidized bed. The Eulerian modeling incorporating the kinetic theory for granular particles coupled with the k-ε turbulence model was developed. The modeling utilized the drying model with a user-defined functions (UDF) for the simulation. The effects of the specularity coefficient and the particle-particle coefficient of restitution (COR) on oil shale particles hydrodynamics, and of the flue gas temperature and velocity on their drying characteristics were studied. It was shown that with a decrease in the specularity coefficient, the particle velocity increased, while the flue gas velocity, pressure drop and wall shear stress decreased. Decreasing the normal COR tended to increase the axial solid velocity fluctuations and the number of the bubbles formed. The predicted pressure drop and moisture content agreed reasonably with the experimental results at COR = 0.9 and the specularity coefficient = 0.2. The temperature and velocity of flue gas were shown to have a great influence on the drying characteristics of oil shale.*

Keywords: *fluidized bed, computational fluid dynamics modeling, hydrodynamics, oil shale drying.*

1. Introduction

With its continuously increasing consumption, the available resources can no longer meet the growing human needs for energy. Oil shale is a special sedimentary rock with a high concentration of organic matter, but it also contains some amounts of inorganic minerals [1]. Known as "man-made oil", this flammable rock consists of dense thin layers. According to literature,

* Corresponding author: e-mail *xlz@dlut.edu.cn*

world oil shale reserves have been estimated at about 500 billion tons, which are mainly distributed in the United States, Russia and China (47.6 billion tons) [2–4]. Oil shale is chiefly used in petrochemical, power and construction industries, but also in other branches. It is directly combusted for electricity or is used for the distillation of shale oil [5–8]. During combustion and distillation, the dense capillary pores in oil shale easily absorb water, which increases its moisture content from 10 to 30% or higher. In the further distillation process, high moisture causes oil shale to break, which increases energy consumption and equipment maintenance costs. Therefore, dehydration and drying of oil shale before recovery and combustion is necessary.

Fluidized bed technology has found widespread application in fields like coal gasification, metallurgical operations, fluid catalytic cracking, solid fuel combustion, incineration, particles drying, etc. [9]. Especially in recent years, new fluidized bed drying technologies have emerged and related laboratory experiments have been carried out [10, 11]. Some laboratorily verified oil shale drying technologies have been successfully introduced into industrial production operations.

Researchers have extended their efforts towards developing a mathematical model to describe the hydrodynamics and drying of materials in fluidized bed. Verma et al. [12] applied a multiphase model to predict the gas-solid flow behavior in fluidized bed, coupling it with the kinetic theory of granular flow (KTGF), a widely accepted constitutive model for simulating the properties of particle flow. The model uses several hydrodynamic parameters to solve the two-fluid model (TFM). The particle-particle coefficient of restitution (COR) is the measurement of energy dissipation during the collisions between particles, which plays an important role in the gas-solid flow behavior in a fluidized bed. Huilin et al. [13] found that the effect of particle-particle interactions was significant for predicting the flow behavior in the bed. Loha et al. [14] applied different COR values to simulate the fluidized bed hydrodynamics. Fede et al. [15] analyzed the effect of COR on the bubbles dynamics in the fluidized bed. The investigators found that decreasing the coefficient tended to increase the formation of bubbles and reduce the bed expansion. The proper wall boundary conditions for gas and solid phases are critical for the correct prediction of hydrodynamics in the fluidized bed. Many researchers have investigated the effect of the specularity coefficient on the flow behavior, including particle velocity, volume fraction and granular temperature in the bubbling fluidized bed, using the TFM approach [16–18]. There have been conducted numerical drying studies as well. Assari et al. [19] established a dry two-dimensional mathematical model based on Euler's method. Ranjbaran et al. [20] simulated the drying process of wet spherical particles in a fluidized bed dryer. Jamaleddine et al. [21] used computational fluid dynamics (CFD) simulations to predict the hydrodynamic and drying processes of wet polyvinyl chloride (PVC) and grit in laboratory and large pneumatic dryers. The above-mentioned works focused on the drying process

and hydrodynamic parameters of granular materials in the fluidized bed. It was found that the Eulerian-Eulerian approach could adequately solve the gas-solid flow system.

Considering the above, in the current work, the effect of the specularity coefficient and coefficient of restitution on particle velocity, volume fraction, granular temperature and bubble state was investigated in the bubbling fluidized bed. The drying of oil shale in a 3-D fluidized bed was studied at the optimum specularity coefficient and coefficient of restitution. The effects of the temperature and velocity of flue gas on the drying characteristics of oil shale were studied. The predicted pressure drop and moisture content across the bed were compared with the experimental results.

2. Experiment description

2.1. Experimental system

In order to study the drying characteristics of oil shale in fluidized bed, the cold and hot state experiments were performed. The oil shale used for the experiments was from the Liu Shu River area in China. A fluidized bed with a cross-sectional area of 100 mm × 500 mm and a height of 400 mm was prepared in the authors' laboratory. The experimental system consisting of apparatus and operation diagram is illustrated in Figure 1.

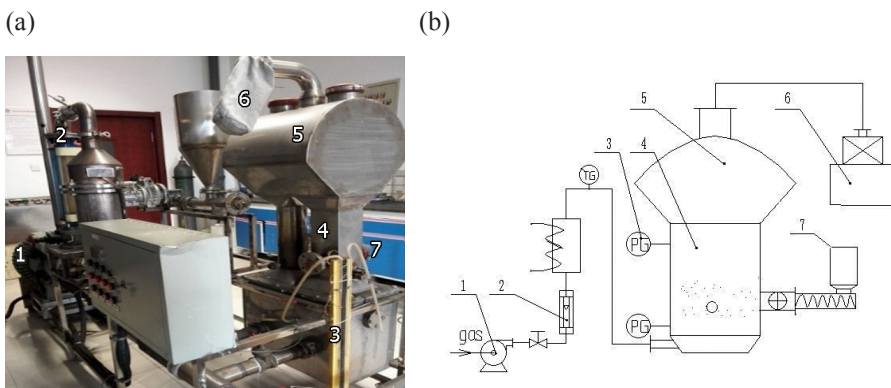(a)   (b)

Fig. 1. Experimental system: (a) apparatus; (b) operation diagram: 1 – blast blower; 2 – rotameter; 3 – mercury U-tube manometer; 4 – fluidized bed; 5 – separator; 6 – bag filter; 7 – AC motor.

2.2. Experimental procedure

The experimental procedure, the operation diagram of which is depicted in Figure 1b, was carried out as follows. The normal temperature air was supplied to the system through the blast blower. The gas flow rate was controlled by the rotameter. The gas passed through the rotameter and flowed into the fluidized bed, which was used to fluidize the oil shale particle. The gas with dust was extracted through the bag filter outside. The pressure drop in the fluidized bed was measured with a mercury U-tube manometer. Table 1 presents the size distribution of oil shale particles. The oil shale sample with the mean specific surface diameter of 2.4 mm was stored in a reservoir and introduced into the fluidized bed by a screw feeder driven by an AC motor.

Table 1. Particle size distribution

Size range, mm	0–2	2–4	4–6
Size distribution, %	47.24	35.55	17.21

The lab-prepared flue gas was used for the hot state experiment. The gas, which was heated to the required temperature by the heater between the rotameter and the mercury U-tube manometer, flowed into the fluidized bed and dried the oil shale particles. The samples were weighed using laboratory sampling equipment, and dried in a temperature-controlled electric oven. The solid phase moisture content was defined as $kg_{(water)}/kg_{(dry\ solid)}$.

3. Numerical simulation description

3.1. Assumption of two-phase flow hydrodynamics model

Based on the theory of TFM and particle dynamics, a numerical model of the drying process of oil shale particles in the fluidized bed was established. This study used the following hypotheses:

(1) Air flow is a transient process and an ideal gas phase is a mixture of flue gas and water vapor.

(2) The solid-phase oil shale is porous, its internal moisture distribution is uniform and particle size is uniform and isotropic.

(3) There occurs a momentum dissipation among the particles or these collide with the wall surface.

(4) The electrostatic force and surface stress occurring during fluidization are ignored.

(5) When the oil shale particles are dried in the fluidized bed, only water evaporates and no shrinkage occurs.

(6) The temperature gradient inside the oil shale particles is ignored.

3.2. Governing equations

In the Eularian-Eularian model approach, both the solid and gas phases are considered to be continuous and fully interpenetrating. The volume fraction of each phase is defined as ε. In the cold fluidization process of the gas-solid flow, the mass conservation of the system occurs. During the drying process mass exchange takes place between the gas (g) and solid (s) phases. The mass conservation equations for the gas and solid phases are written as follows:

$$\frac{\partial}{\partial t}\left(\varepsilon_g \rho_g\right) + \nabla\left(\varepsilon_g \rho_g \overrightarrow{v_g}\right) = m_{sg}, \tag{1}$$

$$\frac{\partial}{\partial t}\left(\varepsilon_s \rho_s\right) + \nabla\left(\varepsilon_s \rho_s \overrightarrow{v_s}\right) = -m_{sg}, \tag{2}$$

where t is the time, v is the velocity, ρ is the density and m is the mass transfer rate.

The momentum balance equations for the gas and solid phases are related by the following equations:

$$\frac{\partial}{\partial t}\left(\varepsilon_g \rho_g \overrightarrow{v_g}\right) + \nabla\left(\varepsilon_g \rho_g \overrightarrow{v_g}\cdot\overrightarrow{v_g}\right) = -\varepsilon_g \nabla P_g + \varepsilon_g \rho_g g + \nabla\cdot\overline{\overline{\tau_g}} + K_{gs}\left(\overrightarrow{v_g}-\overrightarrow{v_s}\right) + m_{sg}\left(v_g - v_s\right), \tag{3}$$

$$\frac{\partial}{\partial t}\left(\varepsilon_s \rho_s \overrightarrow{v_s}\right) + \nabla\left(\varepsilon_s \rho_s \overrightarrow{v_s}\cdot\overrightarrow{v_s}\right) = -\varepsilon_s \nabla P_s + \varepsilon_s \rho_s g + \nabla\cdot\overline{\overline{\tau_s}} + K_{gs}\left(\overrightarrow{v_g}-\overrightarrow{v_s}\right) - m_{sg}\left(v_g - v_s\right), \tag{4}$$

where K is the momentum exchange coefficient, P is the pressure and τ is the stress tensor.

The energy conservation equations for the gas and solid phases are written as:

$$\frac{\partial}{\partial t}\left(\varepsilon_g \rho_g h_g\right) + \nabla\cdot\left(\varepsilon_g \rho_g \overrightarrow{v_g} h_g\right) = -\varepsilon_g \frac{\partial p_g}{\partial t} + \overline{\overline{\tau_g}}:\overrightarrow{\nabla}_g - \nabla\cdot\overrightarrow{q_g} + Q_{sg}, \tag{5}$$

$$\frac{\partial}{\partial t}\left(\varepsilon_s \rho_s h_s\right) + \nabla\cdot\left(\varepsilon_s \rho_s \overrightarrow{v_s} h_s\right) = -\varepsilon_s \frac{\partial p_s}{\partial t} + \overline{\overline{\tau_s}}:\overrightarrow{\nabla}_s - \nabla\cdot\overrightarrow{q_s} + Q_{gs}, \tag{6}$$

where h is the specific enthalpy, q is the heat flow and Q is the heat transfer rate.

3.2.1. Drag models

The drag force between the gas and the solid is one of the dominant forces in a fluidized bed. Different drag models, including Syamlal-O'Brien, Gidaspow and Wen-Yu, are applied to evaluate the effect of interphase momentum exchange between the gas and solid phases in a fluidized bed. The Gidaspow model [22], which has been constructed on the basis of Wen-Yu and Ergun models, is used in the current paper.

3.2.2. The granule kinetic theory

The granule kinetic theory is applied to simulate the flow pattern of particles in the dense phase fluidized bed. The granular temperature (Θ) measures the primary parameters of solid phase movement [18]. It can measure the kinetic energy fluctuation in the solid phase written in terms of the granular fluctuating velocity as:

$$\Theta = \frac{1}{3} v'^2,\tag{7}$$

where v' is the velocity of granular fluctuation. The parameter v' can be governed by the following equation:

$$\frac{3}{2}\left[\frac{\partial}{\partial t}\left(\varepsilon_s \rho_s \Theta\right) + \nabla \cdot \left(\varepsilon_s \rho_s \overrightarrow{v_s}\Theta\right)\right] = \left(-p_s \overline{\overline{I}} + \tau_s\right) : \nabla \overline{v_s} + \nabla \cdot \left(k_\Theta \nabla \Theta\right) - \gamma_\Theta + \phi_{gs},\tag{8}$$

where $\bar{I}$ is the identity tensor, k is the fluctuating energy diffusion, γ is the dissipation of fluctuating energy and ϕ is the fluctuating energy exchange.

The granular pressure P_s is given as:

$$P_s = \varepsilon_s \rho_s \Theta_s + 2\varepsilon_s^2 g_{0,ss}\Theta_s\left(1 + e_{ss}\right),\tag{9}$$

where $g_{0,ss}$ is the radial distribution function and e_{ss} is the the particle-particle coefficient of restitution.

3.2.3. The granular shear viscosity

The granular shear viscosity μ_s results from the tangential force of particles collision composed of collisional, kinetic and frictional components. The solid kinetic, frictional and bulk viscosities are given respectively by Gidaspow, Schaeffer and Lun models used in the present simulation.

3.2.4. Wall condition

For the gas phase, there is usually no-slip wall condition. For the solid phase, the wall boundary condition proposed by Johnson et al. [23] is mostly adopted:

$$v_{s,w} = -A \frac{\partial v_{s,w}}{\partial n}, \tag{10}$$

where A is the slip coefficient, $v_{s,w}$ is the particle slip velocity and n is the unit normal from wall into particle assembly.

The wall shear stress can be expressed as:

$$\vec{\tau}_w = -\frac{\pi}{6} \sqrt{3} \frac{\varepsilon_s}{\varepsilon_{s,max}} \varphi \rho_s \sqrt{\Theta} g_{0,ss} \vec{v}_{s,w}, \tag{11}$$

where φ is the specularity coefficient. The radial distribution function $g_{0,ss}$ defaults to 0.63 in this work.

3.2.5. Drying theory

The energy conservation equations for the gas and solid phases are expressed by Equations (12) and (13):

$$\frac{\partial}{\partial t}\left(\varepsilon_g \rho_g h_g\right) + \nabla \cdot \left(\varepsilon_g \rho_g v_g h_g\right) = -\varepsilon_g \frac{\partial P_g}{\partial t} + \overline{\overline{\tau}}_g : \vec{\nabla} v_g - \nabla \cdot \vec{q}_g + Q_{sg} + \dot{m}\Delta H_{vap}, \tag{12}$$

$$\frac{\partial}{\partial t}\left(\varepsilon_s \rho_s h_s\right) + \nabla \cdot \left(\varepsilon_s \rho_s v_s h_s\right) = -\varepsilon_s \frac{\partial P_s}{\partial t} + \overline{\overline{\tau}}_s : \vec{\nabla} v_s - \nabla \cdot \vec{q}_s + Q_{gs} - \dot{m}\Delta H_{vap}, \tag{13}$$

where ΔH_{vap} is the latent heat of vaporization.

For the gas-solid heat transfer model in the dense phase fluidized bed, it was proposed to use Rowe's, Gunn's and other empirical correlations of heat transfer model based on the Nusselt number. The heat transfer model adopted in this paper for the drying process of oil shale particles in a fluidized bed is as follows [24]:

$$Nu = 0.0114 \, Pr^{1/3} \, Re^{1.625} \left(Re < 100\right), \tag{14}$$

$$Nu = 2 + 1.8 \, Re^{0.5} \, Pr^{1/3} (Re > 100), \tag{15}$$

where Nu is the Nusselt number, Re is the Reynolds number and Pr is the Prandtl number.

The heat exchange coefficient between the gas and the solid is expressed as:

$$h_{sg} = \frac{6\lambda_g \varepsilon_s Nu}{d_s^2}, \tag{16}$$

where λ_g is the thermal conductivity of gas.

The latent heat of wet fraction evaporation is written as follows:

$$\Delta H_{vap} = 3168 - 2.4364 T_s.$$ (17)

When wet oil shale particles come into contact with high temperature flue gas, the particle temperature begins to rise and reaches the evaporation temperature of water. The water on the particle surface evaporates and inside the particle spreads outward. The size and shape of particles as well as the size of their interior voids play a decisive role in the outward diffusion of water. The mass transfer expressions are written as follows [25]:

$$\dot{m} = \frac{kM}{d_s} \left(\frac{P_{sat}(T_s)}{RT_s} - X_{H2O} \frac{P}{RT_g} \right).$$ (18)

The mass transfer coefficient k is solved by the Sherwood number (Sh) as follows:

$$Sh = \frac{kd_s}{D_{vg}} = 2 + 1.8 \, \mathrm{Re}_s^{\,0.5} \, Sc^{1/3},$$ (19)

where D_{vg} is the coefficient of moisture diffusion in the gas phase and Sc is the Schmidt number.

$$D_{vg} = 2.6 \cdot 10^{-5} \cdot \left(\frac{T_s}{288} \right)^{3/2},$$ (20)

where T_s is the temperature of the solid.
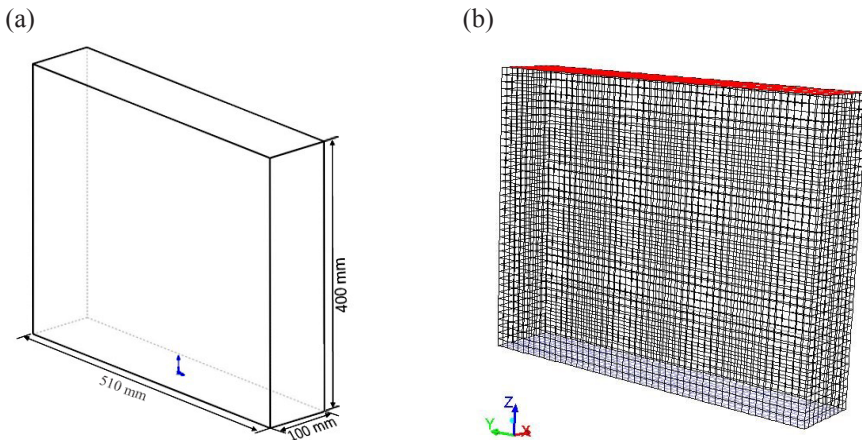
3.3. Simulation setup

Fig. 2. (a) Computational geometry and (b) computational mesh.

A 3-D numerical model based on experimental equipment was created. The geometric model was established with SolidWorks, and GAMBIT program was used to create the computational mesh, which is illustrated in Figure 2. In this study, the 3-D computational simulation was carried out using the control volume-based code FLUENT 17.2. The phase-coupled SIMPLE algorithm was employed to couple the pressure and velocity. Based on the flow condition, the standard k-ε model for CFD simulations was applied in the current work. The basic operation parameters are given in Table 2. The governing and constitutive equations were spatially discretized using a first-order upwind scheme. In order to avoid solution divergence, a transient simulation was adopted using a very small time step, 0.0005 s, with about 30 iterations each step. Convergence occurred when the reported energy fell below 10^{-6} and other variables below 10^{-4}.

Table 2. Physical and operation parameters

Parameter	Value
Apparent particle density, kg/m^3	1270
Average particle size, mm	2.4
Minimum fluidized velocity, m/s	0.946
Superficial gas velocity, m/s	1.64
Static bed height, mm	150
Loose packed voidage	0.45
Particle-particle restitution coefficient (e_{ss})	0.8, 0.9, 0.93, 0.95, 0.98, 1.0
Specularity coefficient (φ)	0.01, 0.05, 0.2, 1.0
Initial moisture content (wet basis)	0.3375
Initial solid temperature, K	300
Flue gas temperature, K	523.15, 573.15, 623.15

3.4. Boundary and initial conditions

The boundary condition at the inlet was used to specify a uniform gas velocity and was injected only in the axial direction. The pressure outlet was set at an ambient atmosphere. Initially, the particles concentration in the bed was

specified and the particle velocity inside the bed was set to zero. The velocity gradients for two phases and the granular temperature gradient of particles along the radial direction were assumed to be zero. For the gas phase the no-slip boundary condition for all walls was assumed, while for the solid phase the Johnson and Jackson boundary condition for all walls was considered. The drying medium was flue gas with parameters given in the study by Xia et al. [25].

3.5. Grid independence test

In the present work, the grid independence study was conducted using grids of three different sizes: a coarse grid of 15 mm, a medium grid of 10 mm and a fine grid of 5 mm. Figure 3 depicts the time-averaged particle volume fraction for grids of different sizes. It was found that the results of the CFD simulation of the flow behavior were quite similar, no matter the size of a grid. A fine grid of 5 mm afforded relatively stable results, but the disadvantage was too long a computational time. Therefore, a medium grid of 10 mm, which could reduce the computational cost and satisfy the accuracy of engineering calculation, was selected for the study.
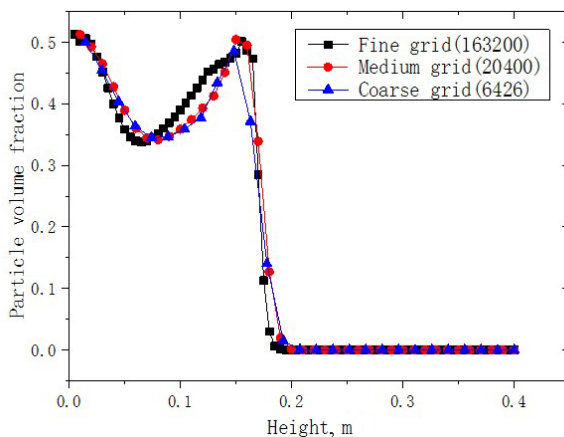

Fig. 3. The time-averaged particle volume fraction for grids of different sizes.

4. Results and discussion

4.1. Comparison between simulation and experiment

The pressure drop and moisture content were simulated and the results were verified with experiment. The simulated pressure drop at a bed height of 150 mm and the moisture content at a gas temperature of 573.15 K within 30 s were compared with experimental measurements, as shown in Figures 4a and 4b, respectively.

(a)   (b)
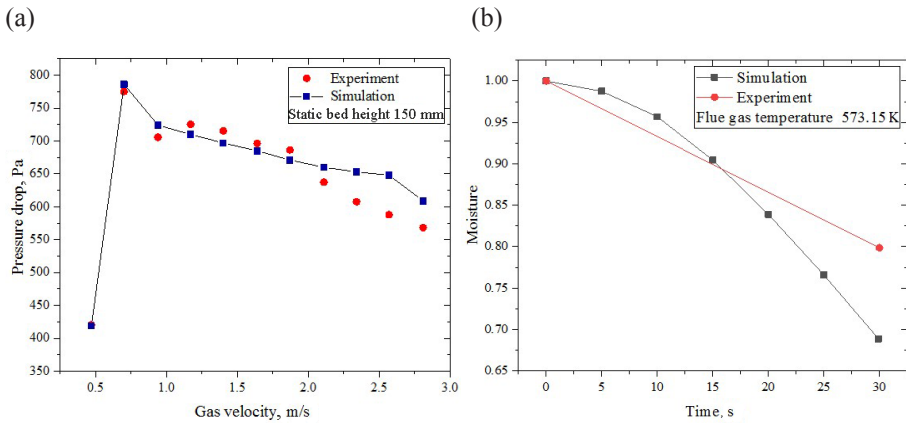

Fig. 4. Comparison between simulated and experimental pressure drops (a) and moisture contents (b).

It can be seen from Figure 4a that the trend of pressure drop with gas velocity is in good agreement with the experimental data, the average relative deviation is 4.17%. At the same time, the simulated moisture content diverges from experimental, the maximum deviation being 13.75%. However, this still satisfies the allowable range of engineering calculation. The mathematical model was shown to be suitable to describe the hydrodynamics and drying parameters of oil shale particles in a fluidized bed.

4.2. Effect of the specularity coefficient on two-phase flow characteristics

The specularity coefficient characterizes the friction between particles and the wall. A strong friction results in a high wall shear stress. Figure 5 illustrates the effect of the specularity coefficient on the vertical distribution of particle volume fraction. The figure displays that the particle volume fraction decreases linearly along the vertical direction with different slopes due to the weight of the solid phase at the bottom of the bed (H < 50 mm). The bed height (50 mm < H < 150 mm), also called a free-board area, is an intersection zone that is randomly changed by the gas pressure. Above the fluidized bed (H > 150 mm), the profile was linear, corresponding to the hydrostatic law for the gas phase, and agreed well with the findings reported by Chang et al. [26]. In the whole fluidized zone, the wall boundary conditions had a little effect on the vertical distribution of the particle volume fraction at COR of 0.9.

The pressure drop across the bed is an important parameter, characterizing the flow behavior in a fluidized bed. Table 3 gives the pressure drop across the bed at different specularity coefficient values. The pressure drop at $\varphi = 0.2$ agreed well with experimental data. The error between the simulation results
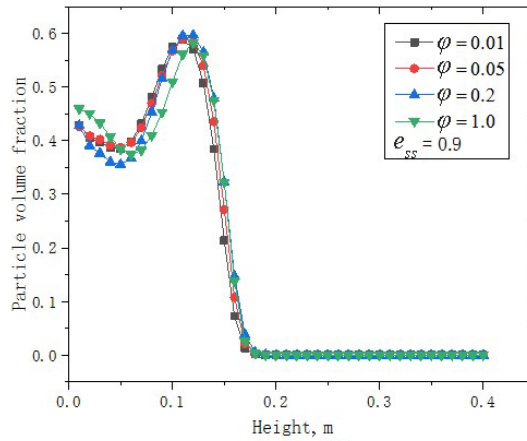
Fig. 5. Vertical distribution of the time-averaged particle volume fraction.

and experimental values was 2.51%, being allowable for later numerical simulation. At the free-slip condition ($\varphi = 0$), it resulted in the smallest pressure drop. With increasing φ, the wall shear stress increased significantly. At $\varphi = 1$, the wall shear stress reached the maximum, 2.05 Pa in the present simulation.

Table 3. The pressure drop across the fluidized bed at different specularity coefficients

Parameter	Simulation					Experimental
Specularity coefficient (φ)	0	0.01	0.05	0.2	1.0	
Wall shear stress, Pa	0	0.07	0.31	1.72	2.05	–
Pressure drop, Pa	578	618	633	685	738	694.6

Figures 6a and 6b show the time-averaged velocity of particles and gas in the radial direction at H = 0.1 m from the inlet, respectively. With increasing specularity coefficient, the radial variation of the particle velocity increased, which coincided with the results obtained by Abdelmotalib et al. [27]. However, the gas velocity decreased.

Figure 7 depicts the radial profiles of the time-averaged solid volume fraction at H = 0.1 m from the inlet at different values of φ. The figure reveals that there was a considerable variation in particle volume fraction and the
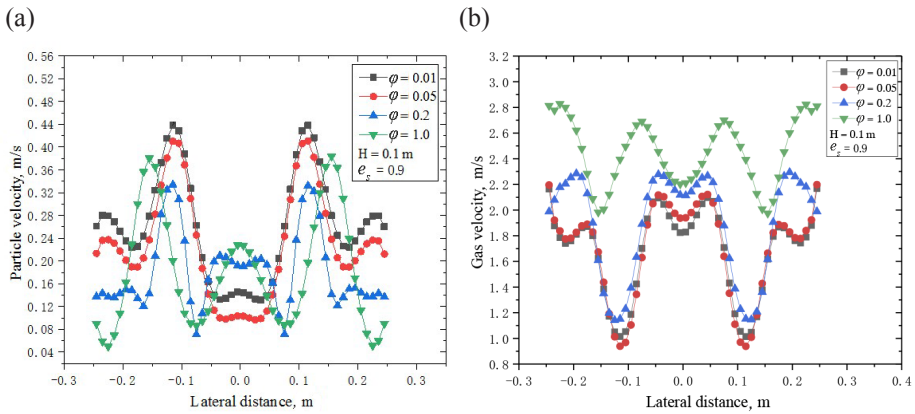
(a)

(b)

Fig. 6. Radial profiles of the time-averaged velocity of particles (a) and gas (b).

particle distribution in the radial direction was not uniform. At the same time, the higher solid volume fraction was neither close to the wall nor at the fluidized bed center. In the whole zone, the uniform fluctuation first decreased and then increased with increasing specularity coefficient. Figure 8 shows the distribution of the solid volume fraction at different specularity coefficients. The figure proves that the specularity coefficient significantly affects the solid flow and bubbling dynamics in the fluidized bed.
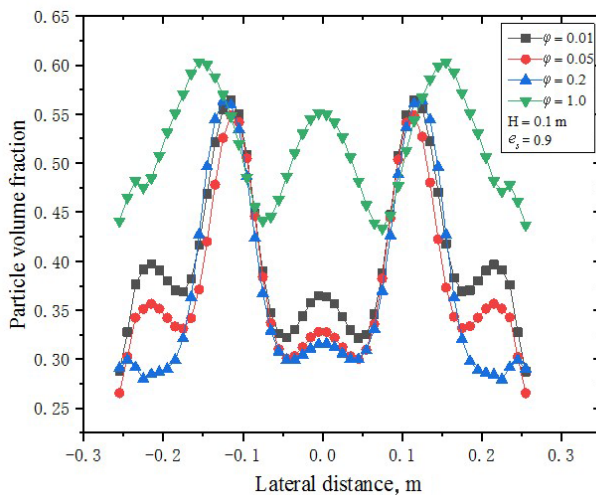
Fig. 7. Radial profiles of the time-averaged solid volume fraction under the wall boundary conditions.
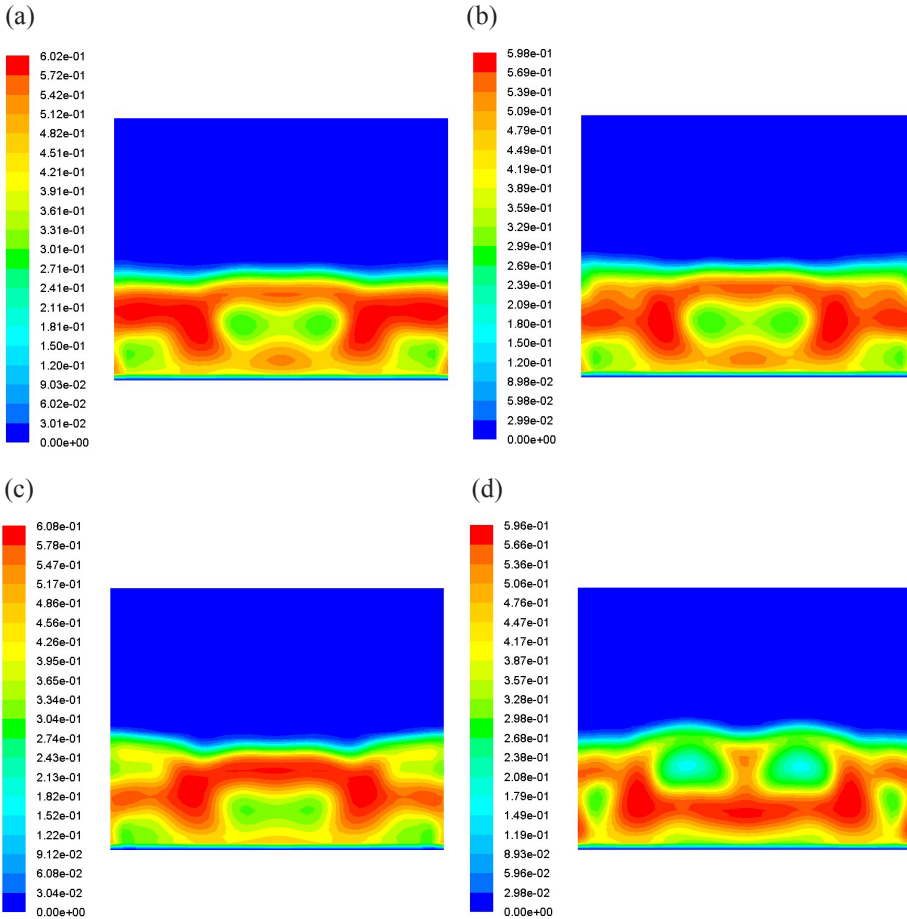
(a)

(b)

(c)

(d)

Fig. 8. Distribution of the solid volume fraction at different specularity coefficients: (a) $\varphi = 0.01$; (b) $\varphi = 0.05$; (c) $\varphi = 0.2$; (d) $\varphi = 1$.

4.3. Effect of the normal particle-particle coefficient of restitution on two-phase flow characteristics

In the numerical simulation of dense gas-solid flows, the particle-particle coefficient of restitution in the Euler-Euler model significantly influences the properties of the solid phase such as solid bulk viscosity, solid pressure and solid shear viscosity, which quantifies the particle-particle collision induced dissipation of kinetic energy. From Table 4 it can be seen that as e_{ss} increases, the pressure drop also increases. When COR is 0.9, the bed pressure drop is in good agreement with the experimental value, the relative error being 2.51%. Thus, the reliability of the model with COR used to predict hydrodynamic parameters is confirmed.

Table 4. The pressure drop across the fluidized bed at different coefficients of restitution ($\varphi = 0.2$)

Coefficient of restitution (e_{ss})	0.8	0.9	0.93	0.95	0.98	1.0	Experimental data
Pressure drop, Pa	613	685	714	733	763	816	694.4

Different COR values (e_{ss} = 0.80, 0.90, 0.93, 0.95, 0.98, 1.0) were used to analyze the flow behavior in the fluidized bed. Figures 9a and 9b show the radial distribution of the time-averaged particle volume fraction at two different bed heights from the inlet: H = 0.1 m (a) and H = 0.05 m (b). The radial distribution of the particle volume fraction is a mirror image of the particle velocity profile. It can be seen from Figure 9 that with increasing COR, the particle volume fraction both near the wall and in the central region of the bed increases and its radial variation decreases. This is due to an increase in the elastic recovery factor, which exacerbates the particle fluctuation in the bed. So, COR significantly influenced the vertical distribution of the solid inside the fluidized bed under given boundary conditions.
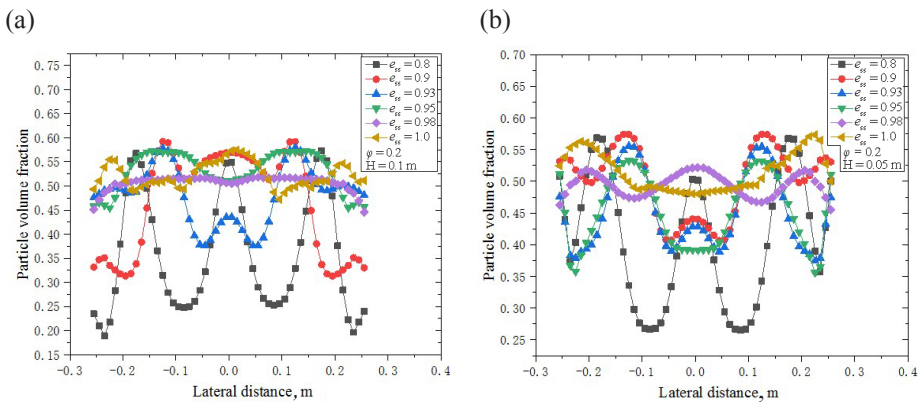
(a)

(b)

Fig. 9. Radial distribution of the time-averaged particle volume fraction at different coefficients of restitution at H = 0.1 m (a) and H = 0.05 m (b) from the inlet.

Figure 10 depicts the instantaneous distribution of the solid phase volume fraction in the fluidized bed at different COR values at the specularity coefficient $\varphi = 0.2$. The study demonstrated that as COR decreased, bigger bubbles were formed in the fluidized bed. It was observed that at COR of from 0.8 to 0.95, the flow behavior showed a core-annulus structure. At the same time, in case of a perfectly elastic collision (e_{ss} = 1.0), no formation of bubbles in the fluidized bed was observed, as a result, there were no fluctuations in

particle velocity. This is in agreement with the finding reported earlier by Fede et al. [15]. A lower value of e_{ss} implied a higher loss of momentum due to an inelastic particle-particle collision, so that the bubble size was larger. As a result, the particles became attached to each other more tightly and a larger void space was generated in the bed.
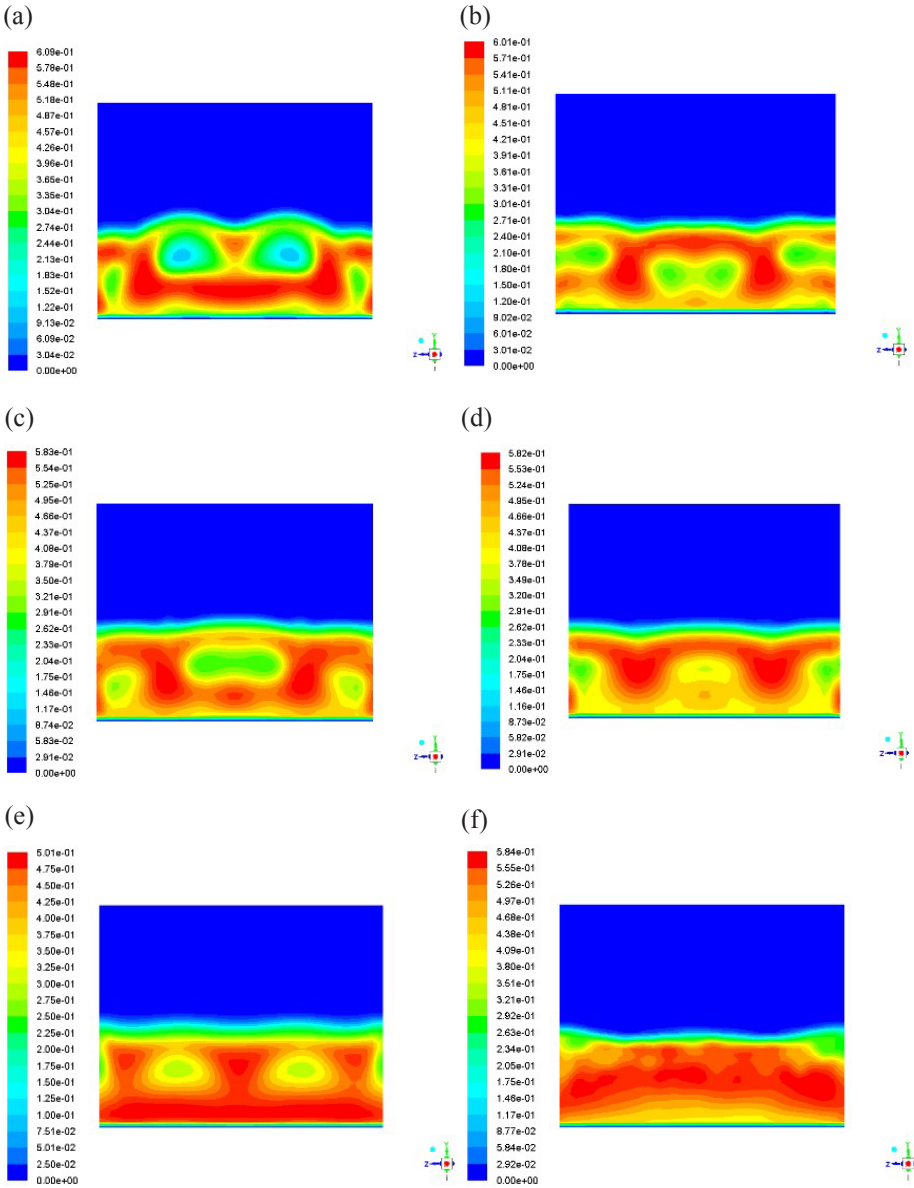
(a)　　　　　　　　　　　　　　　(b)

(c)　　　　　　　　　　　　　　　(d)

(e)　　　　　　　　　　　　　　　(f)

Fig. 10. Distribution of the solid phase volume fraction at different coefficients of restitution at $\varphi = 0.2$: (a) $e_{ss} = 0.8$; (b) $e_{ss} = 0.9$; (c) $e_{ss} = 0.93$; (d) $e_{ss} = 0.95$; (e) $e_{ss} = 0.98$; (f) $e_{ss} = 1.0$.

Figure 11 demonstrates that decreasing the normal COR tended to increase the fluctuations of the solid velocity because there were more and larger bubbles between the particles at a lower COR. This is in agreement with the discovery reported by Hu et al. earlier [28]. Figure 12 illustrates the radial distribution of the time-averaged granular temperature as a function of COR at two different bed heights from the inlet, 0.1 m and 0.08 m. It was observed that the granular temperature was high very close to the wall and then decreased, becoming approximately flat in the central region of the fluidized bed. The granular temperature decreased with decreasing COR because there was a more pronounced dissipation of fluctuating kinetic energy due to the inelastic particle-particle collision. The granular temperature was also observed to increase with decreasing bed height due to the higher-intensity collision.
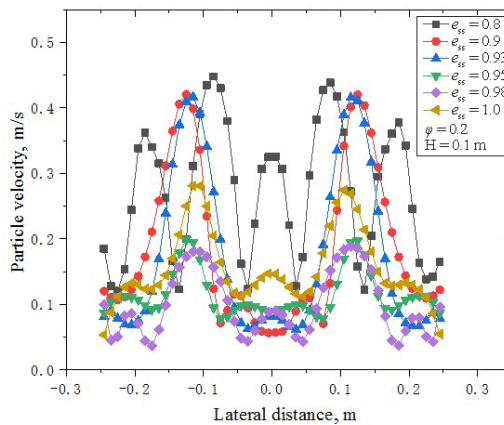

Fig. 11. Radial profiles of the time-averaged axial particle velocity at different coefficients of restitution at H = 0.1 m from the inlet.
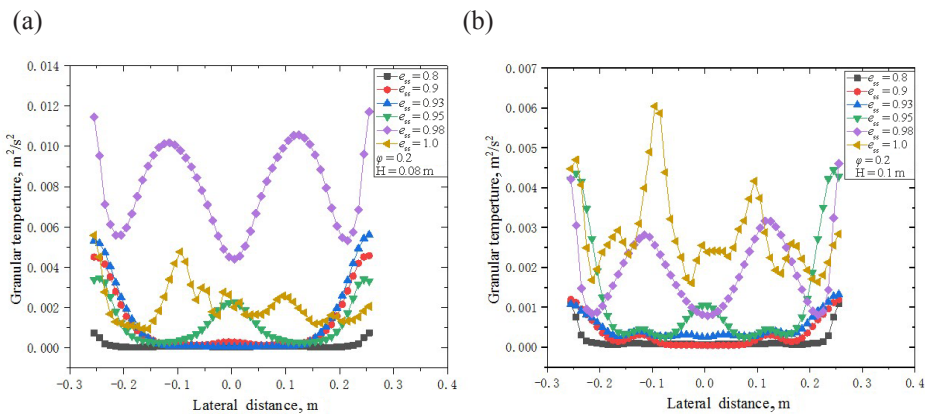
(a)   (b)

Fig. 12. The predicted granular temperature at different particle-particle coefficients of restitution at: (a) H = 0.08 m and (b) H = 0.1 m (b) from the inlet.

4.4. Drying analysis

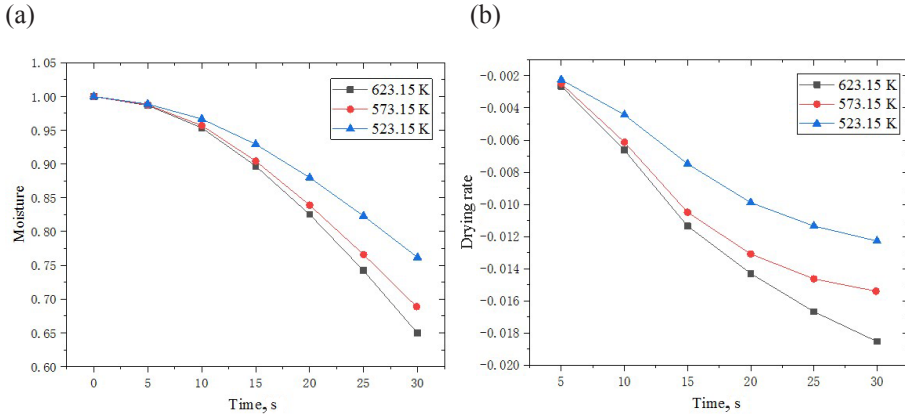(a)   (b)

Fig. 13. The curves of moisture content (a) and drying rate (b) at different temperatures.

Figure 13 shows the curves of moisture content and drying rate at different temperatures. It can be seen that during the same drying time, as the temperature increases, the drying ability of the flue gas becomes stronger, while the moisture content of the oil shale particles decreases to a lesser extent. When the temperature rises from 523.15 to 573.15 K, the decrease in the moisture content is most obvious. The drying rate at different temperatures changes greatly during the same drying time. At 573.15 K the drying rate is relatively stable, which contributes to the stability of the particle drying. Therefore, in the industrial process, the drying temperature of 573.15 K may be considered suitable, to save time and cost.

The moisture profiles at different flue gas temperatures are depicted in Figure 14. The figure reveals that the inlet gas temperature has a great effect on the particle moisture content. As the temperature of the gas increases, the

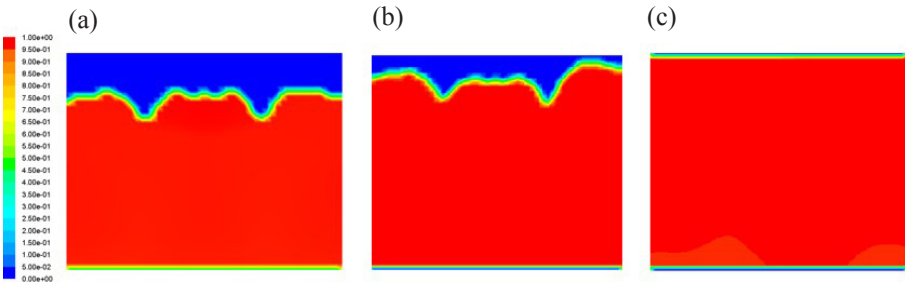(a)   (b)   (c)

Fig. 14. Moisture profiles at different flue gas temperatures at 8 s: (a) 523.15 K; (b) 573.15 K; (c) 623.15 K.

moisture gradually fills the entire bed, which may be caused by the water vapor condensing at the outlet. After that the moisture gradually disappears from the bottom and its content in the particles in the entire bed decreases.

(a)   (b)
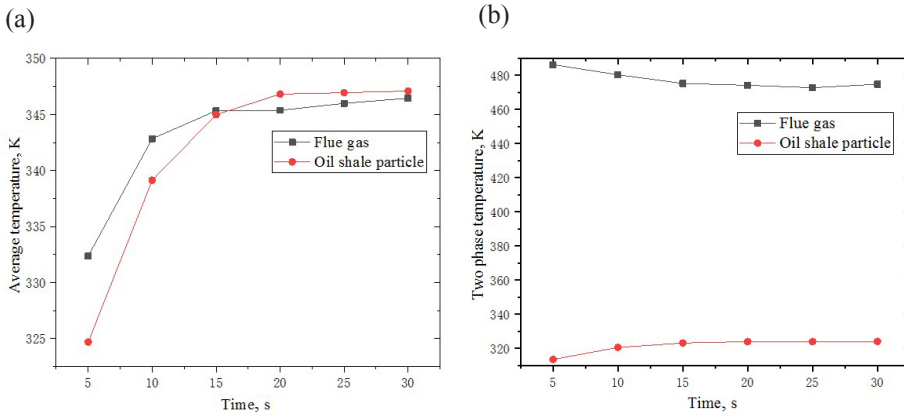

Fig. 15. Temperature profiles of flue gas and oil shale particles with drying time: (a) average temperature in the fluidized bed; (b) two phase temperature distribution at a bed height of 100 mm.

Figures 15a and 15b show the changes of the average temperature of the gas-solid phase in the fluidized bed and the temperature distribution at a bed height of 100 mm with the drying time, respectively. With the increase of the drying time, the average temperature difference between the gas and solid phases in the bed gradually decreases and reaches the same temperature, as shown in Figure 15a. At a bed height of 100 mm from the inlet, the temperature of both the gas phase and the solid phase increases with time in the initial phase

(a)   (b)
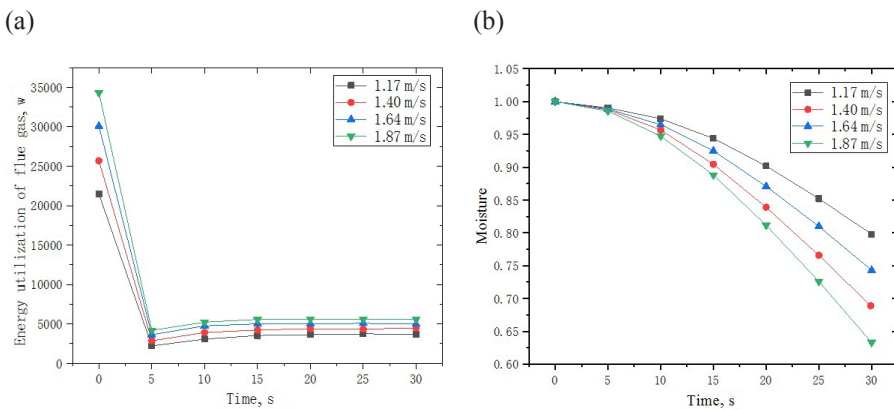

Fig. 16. Effect of the flue gas temperature on: (a) energy consumption and (b) moisture content at different gas velocities.

of the drying process, remaining stable at last. The temperature difference between the two phases is very small, however, the temperature of the gas phase is slightly higher than that of the solid phase, which contributes to the evaporation of particulate water, as shown in Figure 15b.

Figure 16a shows the influence of the flue gas temperature on the energy consumption in the fluidized bed at the gas temperature of 573.15 K. As seen from the figure, the energy consumption in the initial stage of drying is the highest and then gradually stabilizes with the drying time. Increasing the gas velocity will also increase the energy utilization rate. This is because when the flue gas flow increases, the amount of energy entering the drying system will increase, as will the corresponding amount of evaporation moisture. Figure 16b illustrates the variation of the moisture content at different gas velocities. The higher the fluidization speed, the more obvious the moisture content decrease of the particles and the higher the drying rate. The modelling results of the current study were consistent with those obtained by Nabizadeh et al. [29]. Figure 17 shows the distribution of oil shale particles in a fluidized bed at different flue gas velocities at 25 s.
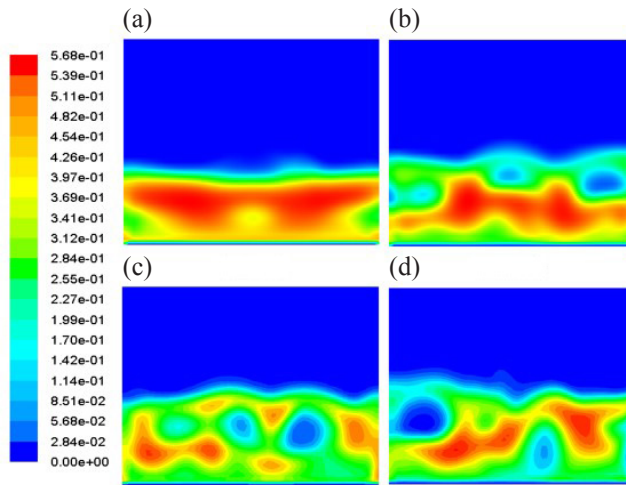

Fig. 17. The distribution of oil shale particles at different flue gas velocities at 25 s: (a) 1.17 m/s; (b) 1.40 m/s; (c) 1.64 m/s; (d) 1.87 m/s.

5. Conclusions

A computational fluid dynamics model was established in a three-dimensional framework to simulate the hydrodynamic and drying characteristics of oil shale particles in a fluidized bed, and was verified by experiments. The simulated pressure drop in the fluidized bed and the moisture content of the particles

were in good agreement with the experimental. The influence of particle-wall boundary conditions and the particle-particle coefficient of restitution on the flow characteristics of oil shale particles was analyzed. The effects of temperature and flue gas velocity on the moisture content of particles and heat and mass transfer were investigated. Based on the results of the study, the following main conclusions can be drawn:

1. With a decrease in the specularity coefficient, the particle velocity increased, while the gas velocity, pressure drop and wall shear stress decreased. At the specularity coefficient of 1.0, the particles stuck to the wall, and thus the shear stress reached the maximum, 2.05 Pa in the present simulation. The predicted pressure drop at the specularity coefficient of 0.2 agreed well with the experimental data.

2. With an increase in the coefficient of restitution, the particle volume fraction both near the wall and in the central region of the fuidized bed increased, while the change in radial direction became less obvious. The granular temperature was high close to the wall and then decreased and became approximately flat in the central region of the bed. Decreasing the normal coefficient of restitution tended to increase the fluctuations of the axial solid velocity, as a result, the number of the bubbles formed increased. The simulated pressure drop values agreed well with the experimental data at the coefficient of restitution of 0.9.

3. The temperature and velocity of flue gas had a great influence on the drying of oil shale. The higher the temperature and the higher the gas velocity, the higher the drying effect. As the temperature increased, the moisture content of the particles decreased to a lesser extent, and the drying temperature of 573.15 K appeared to be more suitable. During the drying process, the energy consumption was much higher in the early stage than in the later stage.

This study is the first step towards providing a deeper understanding of the flow and heat and mass transfer processes in a three-dimensional oil shale fluidized bed. For scaling-up more experimental data and further computational fluid dynamics studies will be required.

REFERENCES

1. Dyni, J. R. Geology and resources of some world oil-shale deposits. *Oil Shale*, 2003, **20**(3), 193–252.
2. Wang, Q., Bo, J. R., Sun, B. Z., Sun, J. Strategy of Huadian oil shale comprehensive utilization. *Oil Shale*, 2005, **22**(3), 305–315.
3. Han, X., Kulaots, I., Jiang, X., Suuberg, E. M. Review of oil shale semicoke and its combustion utilization. *Fuel*, 2014, **126**, 143–161.
4. Liu, Z. J., Dong, Q. S., Ye, S. Q. The situation of oil shale resources in China. *Journal of Jilin University (Earth Science Edition)*, 2006, **36**(6), 869–876 (in Chinese with English abstract).

5. Li, X., Zhou, H., Wang, Y., Qian, Y., Yang, S. Thermoeconomic analysis of oil shale retorting processes with gas or solid heat carrier. *Energy*, 2015, **87**, 605–614.

6. Aboulkas, A., El Harfi, K., El Bouadili, A., Nadifiyine, M., Benchanaa, M. Study on the pyrolysis of Moroccan oil shale with poly (ethylene terephthalate). *J. Therm. Anal. Calorim.*, 2010, **100**(1), 323–330.

7. Al-Harahsheh, M., Al-Ayed, O., Robinson, J., Kingman, S., Al-Harahsheh, A., Tarawneh, K., Saeid, A., Barranco, R. Effect of demineralization and heating rate on the pyrolysis kinetics of Jordanian oil shales. *Fuel. Process. Technol.*, 2011, **92**(9), 1805–1811.

8. Janković, B. The kinetic modeling of the non-isothermal pyrolysis of Brazilian oil shale: Application of the Weibull probability mixture model. *J. Petrol. Sci. Eng.*, 2013, **111**, 25–36.

9. Lv, W., Li, S., Han, Q., Zhao, Y., Wu, H. Study of the drying process of ginger (*Zingiber officinale* Roscoe) slices in microwave fluidized bed dryer. *Dry. Technol.*, 2016, **34**(14), 1690–1699.

10. Naz, M. Y., Sulaiman, S. A., Bou-Rabee, M. A. Particle tracking velocimetry investigations on density dependent velocity vector profiles of a swirling fluidized bed. *Dry. Technol.*, 2017, **35**(2), 193–202.

11. Bennamoun, L., Chen, Z., Afzal, M. T. Microwave drying of wastewater sludge: Experimental and modeling study. *Dry. Technol.*, 2016, **34**(2), 235–243.

12. Verma, V., Deen, N. G., Padding, J. T., Kuipers, J. A. M. Two-fluid modeling of three-dimensional cylindrical gas–solid fluidized beds using the kinetic theory of granular flow. *Chem. Eng. Sci.*, 2013, **102**, 227–245.

13. Huilin, L., Yurong, H., Gidaspow, D. Hydrodynamic modelling of binary mixture in a gas bubbling fluidized bed using the kinetic theory of granular flow. *Chem. Eng. Sci.*, 2003, **58**(7), 1197–1205.

14. Loha, C., Chattopadhyay, H., Chatterjee, P. K. Effect of coefficient of restitution in Euler-Euler CFD simulation of fluidized-bed hydrodynamics. *Particuology*, 2014, **15**, 170–177.

15. Fede, P., Simonin, O., Ingram, A. 3D numerical simulation of a lab-scale pressurized dense fluidized bed focussing on the effect of the particle-particle restitution coefficient and particle–wall boundary conditions. *Chem. Eng. Sci.*, 2016, **142**, 215–235.

16. Loha, C., Chattopadhyay, H., Chatterjee, P. Euler-Euler CFD modeling of fluidized bed: Influence of specularity coefficient on hydrodynamic behavior. *Particuology*, 2013, **11**(6), 673–680.

17. Zhong, H., Gao, J., Xu, C., Lan, X. CFD modeling the hydrodynamics of binary particle mixtures in bubbling fluidized beds: Effect of wall boundary condition. *Powder Technol.*, 2012, **230**, 232–240.

18. Lan, X., Xu, C., Gao, J., Al-Dahhan, M. Influence of solid-phase wall boundary condition on CFD simulation of spouted beds. *Chem. Eng. Sci.*, 2012, **69**(1), 419–430.

19. Assari, M. R., Tabrizi, H. B., Saffar-Avval, M. Numerical simulation of fluid bed drying based on two-fluid model and experimental validation. *Appl. Therm. Eng.*, 2007, **27**(2–3) 422–429.

20. Ranjbaran, M., Zare, D. CFD modeling of microwave-assisted fluidized bed drying of moist particles using two-fluid model. *Dry. Technol.*, 2012, **30**(4), 362–376.

21. Jamaleddine, T. J., Ray, M. B. Drying of sludge in a pneumatic dryer using computational fluid dynamics. *Dry. Technol.*, 2011, **29**(3), 308–322.

22. Gidaspow, D., Bezburuah, R., Ding, J. Hydrodynamics of circulating fluidized beds: Kinetic theory approach. *Proceedings of the 7th International Conference on Fluidization*, Gold Coast (Australia), 3–8 May 1992.

23. Johnson, P. C., Jackson, R. Frictional–collisional constitutive relations for granular materials with application to plane shearing. *J. Fluid Mech.*, 1987, **176**, 67–93.

24. Paláncz, B. A mathematical model for continuous fluidized bed drying. *Chem. Eng. Sci.*, 1983, **38**(7), 1045–1059.

25. Xia, L., Zhang, H., Wang, B., Yu, C., Fan, X. Experimental and numerical analysis of oil shale drying in fluidized bed. *Dry. Technol.*, 2017, **35**(7), 802–814.

26. Chang, J., Wu, Z., Wang, X., Liu, W. Two- and three-dimensional hydrodynamic modeling of a pseudo-2D turbulent fluidized bed with Geldart B particle. *Powder Technol.*, 2019, **351**, 159–168.

27. Abdelmotalib, H., Youssef, M. A. M., Hassan, A. A., Youn, S. B., Im, I.-T. Influence of the specularity coefficient on hydrodynamics and heat transfer in a conical fluidized bed combustor. *Int. Commun. Heat. Mass.*, 2016, **75**, 169–176.

28. Hu, C., Luo, K., Wang, S., Junjie, L., Fan, J. The effects of collisional parameters on the hydrodynamics and heat transfer in spouted bed: A CFD-DEM study. *Powder Technol.*, 2019, **353**, 132–144.

29. Nabizadeh, A., Hassanzadeh, H., Asadieraghi, M., Hassanpour, A., Moradi, D., Moraveji, M. K., Namin, M. H. A parametric study of the drying process of polypropylene particles in a pilot-scale fluidized bed dryer using Computational Fluid Dynamics. *Chem. Eng. Res. Des.*, 2020, **156**, 13–22.